中国光学（中英文） Chinese Optics 核心期刊

通过磁表面等离激元的多重相干提高灵敏度

杨宗蒙 邢前 陈怡安 侯玉敏

Improving sensitivity by multi-coherence of magnetic surface plasmons

YANG Zong-meng, XING Qian, CHEN Yi-an, HOU Yu-min

引用本文:
杨宗蒙, 邢前, 陈怡安, 侯玉敏. 通过磁表面等离激元的多重相干提高灵敏度[J]. 中国光学, 2023, 16(2): 458-465. doi: 10.37188/CO.EN.2022-0009
YANG Zong-meng, XING Qian, CHEN Yi-an, HOU Yu-min. Improving sensitivity by multi-coherence of magnetic surface plasmons[J]. *Chinese Optics*, 2023, 16(2): 458-465. doi: 10.37188/CO.EN.2022-0009

在线阅读 View online: https://doi.org/10.37188/CO.EN.2022-0009

文章编号 2097-1842(2023)02-0458-08

Improving sensitivity by multi-coherence of magnetic surface plasmons

YANG Zong-meng, XING Qian, CHEN Yi-an, HOU Yu-min*
(*State Key Laboratory of Artificial Microstructure and Mesoscopic Physics*, *School of Physics*, *Peking University*, *Beijing* 100871, *China*)
* *Corresponding author*, *E-mail*: *ymhou@pku.edu.cn*

Abstract: In this paper, we study the coherence of magnetic surface plasmons in one-dimensional metallic nano-slit arrays and propose a double-dip sensing method to improve sensitivity. Different from the conventional way of scanning wavelength at a fixed incident angle, coherence of surface plasmons is investigated by changing the incident angle at a fixed wavelength. Due to the retardation effect, two coherence dips move in opposite directions as the refractive index of the surrounding medium changes. Compared with one dip used for sensing, two oppositely moving dips can efficiently improve the sensitivity. The total sensitivity of two dips can reach 141.6°/RIU while the sensitivities of two single dips are 39.2°/RIU and 102.4°/RIU respectively. Besides, the inconsistency between the refractive index of slit medium and upper medium has few influences on the sensing performance, which will have wide practical applications.
Key words: surface plasmons; refractive index sensor; coherence; metal grating

通过磁表面等离激元的多重相干提高灵敏度

杨宗蒙, 邢 前, 陈怡安, 侯玉敏*
（北京大学 物理学院, 人工微结构与介观物理国家重点实验室, 北京 100871）

摘要: 本文研究了一维金属纳米狭缝阵列中磁表面等离激元的相干现象, 并提出了一种双谷传感方法以提高灵敏度。与通常所采用的固定入射角度进行波长扫描的方式不同, 本文采用固定波长改变入射角度的方式研究表面等离激元的相干现象。由于延迟效应的存在, 随着周围介质折射率的变化, 两个谷会向相反的方向移动。相比于使用单一谷进行标定的方式, 两个相反方向移动的谷可以有效提高灵敏度。用于标定的两个谷单独的灵敏度最大分别为 39.2°/RIU 和 102.4°/RIU, 而双谷标定的总灵敏度可达 141.6°/RIU。此外, 狭缝介质与上层介质的折射率不一致对传感性能的影响很小, 故其有广泛的应用前景。
关 键 词: 表面等离激元; 折射率传感器; 相干; 金属光栅
中图分类号: O482.31 **文献标志码:** A **doi:** 10.37188/CO.EN.2022-0009

收稿日期: 2022-05-24; **修订日期:** 2022-06-20
基金项目: 国家自然科学基金 (No. 61575006)
Supported by National Natural Science Foundation of China (No. 61575006)

1 Introduction

Surface Plasmon (SP) —collective oscillation of free electrons along a metal surface, is mainly divided into two categories: Surface Plasmon Polaritons (SPPs) and Localized Surface Plasmons (LSPs)[1-2]. They are widely utilized in surface-enhanced spectroscopy, biochemical sensors[3-4], nonlinear optics[5], lasers[6], optical lenses[7] and so on. Due to the wave vector mismatch between SPPs and light in free space, SPPs can be excited in structures such as the Kretschmann configuration[8-10]. While LSPs can be directly excited by light in free space and their resonance frequencies are able to be tuned by the shapes of metallic nanoparticles[11-14]. However, radiation loss of LSPs results in a large linewidth that significantly limits the potential applications of LSPs [15].

According to the research, the relative phase difference generated by oblique incidence and retardation effect affects the interaction between LSPs. And it is demonstrated in suspended metallic nano-sandwich arrays that the coherence condition of LSPs is the same as Wood-Rayleigh anomaly[16-18]. Fano resonance occurs when a discrete state couples to a continuum state and forms a typical asymmetric line shape in the spectrum[19-21]. Thus, the coherence of LSPs at specific resonance wavelength and incident angle can be observed via Fano resonance. This phenomenon is also known as plasmonic lattice resonance or Surface Lattice Resonance (SLR)[22-24]. Because SLR has narrower linewidth and higher Q factor than LSPs of individual particles, it provides a number of applications in areas such as refractive index sensing[25-27], color printing[28, 29], optical filter[30] and fluorescence enhancement[31]. Commonly, SLR is investigated in the wavelength-dependent spectra when the incident angle is fixed. SHEN Y *et al.*[32], for example, proposed a metallic mushroom arrays structure composed of gold caps, photoresist pillars and gold holes, and got hybridized mode of Wood-Rayleigh anomaly and localized surface plasmon. The sensitivity and FOM of that sensor can reach 1 015 nm/RIU and 108/RIU, respectively.

In this paper, we investigate the coherence of LSPs in one-dimensional metallic nano-slit arrays built on a sapphire substrate and derive coherence equations for different dielectric-metal interfaces. Due to magnetic surface plasmon resonance, the ring current driven by external electromagnetic field can induce magnetic field enhancement in the slits. A vertical Metal-Insulator-Metal (MIM) sandwich structure is made by metal and dielectric slit, which can be regarded as a Magnetic Resonator (MR). It also can be understood as the combination of capacitors and inductors in LC circuit[33-35]. Just like X-ray diffraction, we rotate the incident angle to achieve two directional coherent states corresponding to the interface between metal and upper medium, as seen by two dips in angle-resolved spectrum. As the refractive index of the upper medium changes, the two coherence dips shift in opposite directions due to the retardation effect. Compared with using a single dip for sensing, two oppositely moving dips can effectively improve sensitivity.

2 Structure and method

Fig. 1(a) (color online) shows the proposed structure which is periodic in *x*-direction and infinite in *z*-direction. The width and thickness of Au slabs are a=990 nm and b=170 nm, respectively. The period of the structure is P=1000 nm and the slit width is d=10 nm. The refractive index of the sapphire substrate is n_s = 1.77, and the surrounding medium is water and n_w = 1.33. The proposed structure can be fabricated by atomic layer lithography[36-37]. TM polarized light, whose magnetic field component is along the *z* direction, illuminates in *xy* plane at an incident angle of θ.

The simulation tool in this paper is commercial software COMSOL Multiphysics 5.6 based on finite element method. To simplify, we use two-dimensional model and set periodic condition in *x*-dir-

ection. The wavelength-dependent complex dielectric constants of Au are taken from experimental data in ref [38].

3 Results and discussion

Firstly, the reflection spectrum of the structure under normal incidence ($\theta = 0°$) with wavelength ranging from 1 000 nm to 1 700 nm is shown in Fig. 1(b) (color online). It can be seen a broad dip 1 and a sharp dip 2 are located at 1 272 nm and 1 388 nm, respectively. The normalized magnetic field intensity distributions ($|H|/|H_0|$) at dip 1 and dip 2 are depicted in Figs. 1(c) (color online) and 1(d) (color online), respectively. The red arrows in Figs. 1(c)~1(d) are proportional to the current density. As can be seen in both Figs. 1(c) and 1(d), the ring current excited in metal produces large magnetic field enhancement in the slit. But for dip1, it originates from magnetic surface plasmon resonance. For dip 2, it is typically asymmetric Fano line-shape caused by the coupling between magnetic surface plasmon resonance mode and the coherent state.

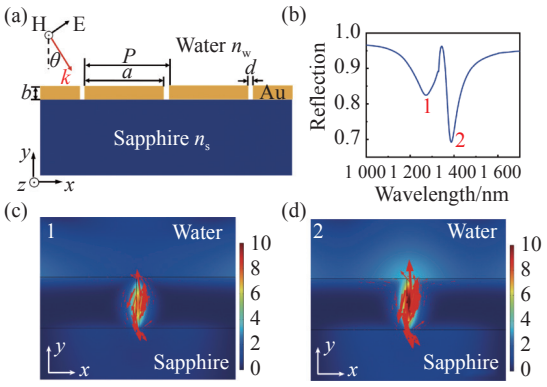

Fig. 1 (a) Schematic diagram of one-dimensional metallic nano-slit arrays structure on sapphire substrate. The whole structure is immersed in water; (b) the reflection spectrum at normal incidence; (c)(d) the normalized magnetic field intensity distributions corresponding to the dip 1 and dip 2, respectively

In order to analyze the coherence conditions of magnetic surface plasmon resonance in this structure, we consider the interaction of two neighboring magnetic resonators. As shown in Fig. 2(color online), the purple and green balls in the slits represent magnetic resonators MR 2 and MR 1, respectively. And the relative phase difference between them caused by oblique incidence is $\varphi_0 = -2\pi P n_w \sin\theta/\lambda$, where λ is incident wavelength in vacuum. The contact between two MRs is mediated by the SPP wave since MR2 and MR1 are connected by metal. The retardation phase difference in Figs. 2(a) and 2(b) are $\varphi_{21} = \pm 2\pi P/\lambda_{SPP}^{water}$ and $\varphi'_{21} = \pm 2\pi P/\lambda_{SPP}^{sub}$, in which λ_{SPP}^{water} and λ_{SPP}^{sub} are the wavelengthes of SPP along the metal surfaces adjacent to water and substrate, respectively ("±" indicates the wave propagates along $+x$ or $-x$ direction, shown as black or white arrows in Fig. 2). Thus, the correlated phase difference between MRs in above two cases are $\Delta\varphi = \varphi_0 + \varphi_{21}$ and $\Delta\varphi' = \varphi_0 + \varphi'_{21}$. The coherence of magnetic surface plasmon resonance is achieved when the correlated phase difference meets $2m\pi$ or $2l\pi$ (m or l is an integer). Then we can get coherence equations written as

$$P\left(\pm\sqrt{\frac{n_w^2\varepsilon_m}{n_w^2+\varepsilon_m}} - n_w\sin\theta\right) = m\lambda \quad , \qquad (1)$$

$$P\left(\pm\sqrt{\frac{n_s^2\varepsilon_m}{n_s^2+\varepsilon_m}} - n_w\sin\theta\right) = l\lambda \quad , \qquad (2)$$

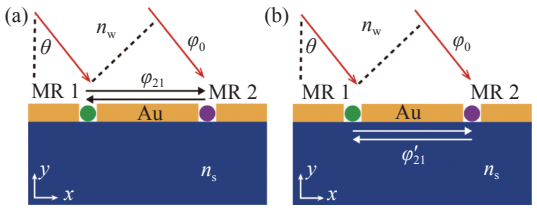

Fig. 2 Analysis of the phase difference between neighboring magnetic surface plasmon resonances in one-dimensional metallic nano-slit arrays in (a) water and (b) substrate. The red arrows represent the incident light

where ε_m is the permittivity of metal. The process of calculability can refer to ref [16]. The coherence conditions of SPP along metal surfaces adjacent to water and substrate are described by Eq. (1) and Eq. (2), respectively. And + (−) means coherence along $+x$ ($-x$) direction, corresponding to $m > 0$, $l > 0$

($m<0$, $l<0$). According to the calculation results of Eq. (1), when $\theta=0°$, coherence of MRs along the $+x$ and $-x$ directions exists simultaneously at a specific wavelength and a standing wave is formed adjacent to the interface between metal and water which is shown by Fig. 1(d). The interaction of magnetic surface plasmon resonance with the coherent state results in Fano resonance as dip 2 shown in Fig. 1(b).

To further investigate the coherent phenomenon in this structure, both the wavelength and the incident angle are varied (λ is from 1 000 nm to 1 700 nm, θ is from 0° to 60°).

The 2D reflectance spectrum is shown in Fig. 3 (a) (color online). The calculated coherence conditions of the upper metal interface are drawn with dashed lines named $C_{m=-1}^{\text{water}}$ $C_{m=1}^{\text{water}}$ and $C_{m=-2}^{\text{water}}$, respectively, and those of the lower metal interface calculated by Eq. (2) are drawn with solid lines named $C_{l=-2}^{\text{sub}}$ and $C_{l=1}^{\text{sub}}$, respectively. A dark broad band (approximately from 1 215 nm to 1 400 nm) between two vertical green dashed lines in Fig. 3(a) originates from magnetic surface plasmon resonance. Other narrow bands result from the coherence of surface plasmons. As it can be seen, the calculated coherence lines match well with the simulation results, except for the region between two vertical green lines due to the strong interaction between coherence and surface plasmon resonance.

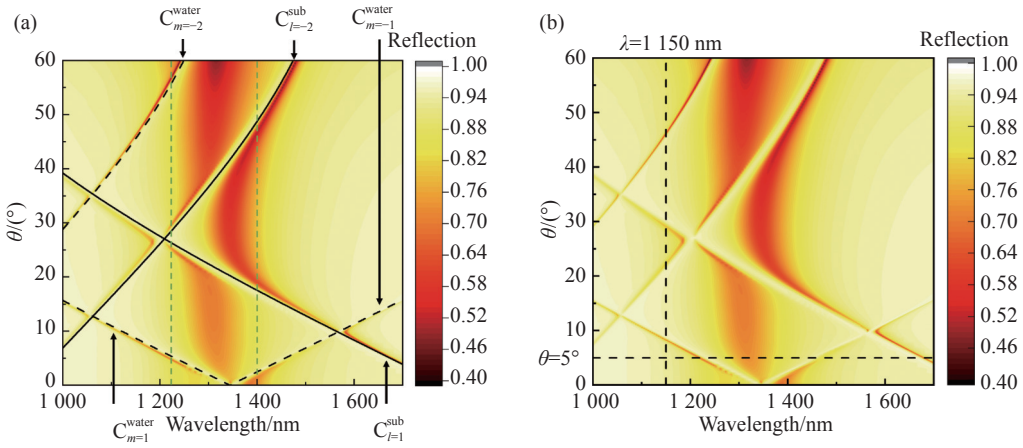

Fig. 3　2D Reflection spectra of the structure in the range of $\theta=0\sim60°$ and $\lambda=1\,000\sim1\,700$ nm. (a) Three dashed lines $C_{m=-1}^{\text{water}}$, $C_{m=1}^{\text{water}}$, and $C_{m=-2}^{\text{water}}$ represent different orders of magnetic surface plasmon coherence corresponding to the interface between metal and water, respectively. Two solid lines $C_{l=-2}^{\text{sub}}$ and $C_{l=1}^{\text{sub}}$ represent different orders of coherence corresponding to the interface between metal and substrate; (b) positions of fixed wavelength $\lambda=1150$ nm and fixed incident angle $\theta=5°$ are marked by vertical and horizontal dashed lines in 2D spectrum, respectively

We take $\lambda=1\,150$ nm (position marked by vertical dashed line in Fig. 3(b) (color online)) and change the incident angle to explore several coherent states. In Fig. 4(a) (color online), four coherent states named A, B, C and D are shown by the reflection dips in angle-resolved spectrum. Moreover, the normalized magnetic field intensity distributions of these states are drawn in Fig. 4(b) (color online). The black arrows are proportional to Poynting vectors. From A and B, it can be seen that the near fields are mainly localized above the upper surface of metal due to the coherent states of SPP adjacent to water. Based on Eq. (1), A ($m=1$) and B ($m=-2$) are the coherent states along $+x$ and $-x$ directions, which is confirmed by the energy flow. Similarly, C ($l=-2$) and D ($l=1$) are the coherent states of SPP adjacent to the substrate along $-x$ and $+x$ directions.

According to the two variables λ and θ in Eq. (1), there are two ways to realize refractive index sensing: wavelength interrogation and incident angle interrogation. And there are two sensitivity

definitions $S_\lambda = \Delta\lambda/\Delta n$ and $S_\theta = \Delta\theta/\Delta n$, in which the latter is used in this work. Because wavelength interrogation is conventionally used in previous work[25-27, 32], it is necessary to derive the relation between S_λ and S_θ. In the wavelength range of 1000 ~ 1700 nm, $\sqrt{\varepsilon_m/(n_w^2+\varepsilon_m)}$ can be approximated to 1, because $|\varepsilon_m| \gg n_w^2$ (the value of $\sqrt{\varepsilon_m/(n_w^2+\varepsilon_m)}$ varies from 1.006 to 1.023 in this range when n_w = 1.33). So, Eq. (1) can be simplified as:

$$P(\pm n_w - n_w \sin\theta) = m\lambda \quad . \tag{3}$$

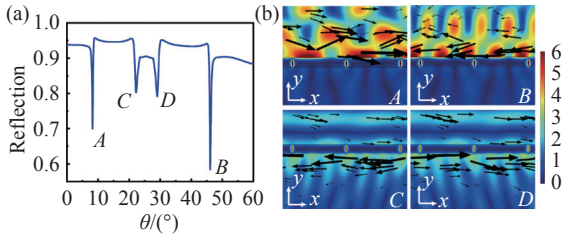

Fig. 4 (a) Angle-resolved reflection spectrum at a fixed incident wavelength of 1 150 nm. (b) The four graphs show the normalized magnetic field intensity distributions corresponding to the four dips *A*, *B*, *C* and *D* appearing in (a), respectively. Black arrows represent the Poynting vectors

From Eq. (3), we can deduce the relation between the two sensitivity definitions:

$$S_\theta = \frac{m}{n_w P \cos\theta} S_\lambda \quad . \tag{4}$$

Next, we change the refractive index of the upper medium to study the sensing performance of this structure. As shown in Fig. 5(a) (color online), with the increase of the refractive index n_w, dip *A* and dip *B* move in opposite directions. We take θ_A and θ_B as the angles corresponding to dip *A* and dip *B*, respectively. The reverse movement can be seen intuitively in Fig. 5(b) (color online). When λ is fixed and n_w becomes larger, the coherent states of *A* and *B* take positive and negative signs in Eq. (1), resulting in larger θ_A and smaller θ_B, respectively. While in Eq. (2), "±" sign related term remains unchanged, and the increase of n_w will inevitably lead to decrease of θ. As a result, the angles of both dip *C* and *D* (θ_C, θ_D) are slightly shifted to small values as n_w increases. However, as demonstrated in Fig. 5(c) (color online), wavelength interrogation cannot lead to reverse movement of double dips. In this case, the incident angle is $\theta = 5°$ (position marked by horizontal dashed line in Fig. 3(b)) and the two dips are caused by coherence of $m = 1$ and $m = -1$ corresponding to interface between metal and upper medium.

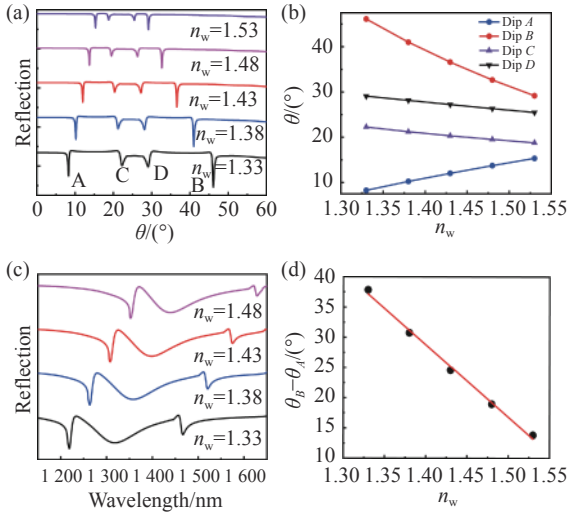

Fig. 5 (a) The angle-resolved reflectance spectrum obtained by changing the refractive index of the upper medium (n_w=1.33 ~ 1.53) with an interval of 0.05 at the wavelength of 1 150 nm. (b) Dip position varying with the refractive index. (c) Reflection spectrum is obtained by changing the wavelength when θ is fixed at 5°. As the refractive index increases, both coherence dips are red-shifted. (d) The angle difference between dip *A* and dip *B* varying with the upper medium

We define the total sensitivity of two dips as:

$$S = \Delta(\theta_A - \theta_B)/\Delta n_w \quad . \tag{5}$$

According to the analysis above, we can infer that $\Delta\theta_A/\Delta n_w > 0$ and $\Delta\theta_B/\Delta n_w < 0$. The sensitivities of dip *A* and dip *B* are $S_A = |\Delta\theta_A/\Delta n_w| = \Delta\theta_A/\Delta n_w$ and $S_B = |\Delta\theta_B/\Delta n_w| = -\Delta\theta_B/\Delta n_w$, respectively. As a result, the total sensitivity $S = S_A + S_B$ is better than the sensitivity of any single dip. Since dip *A* and dip *B* have different sensitivity and FWHM, we calculate their FOMs separately. The definitions of FOMs are $FOM_A = S_A/FWHM_A$ and $FOM_B = S_B/FWHM_B$. Sensitivities and FOMs of different refractive index are listed in Table 1. The

maximum sensitivities of two single dips are 39.2°/RIU and 102.4°/RIU and the corresponding FOMs are 115.2/RIU and 214.1/RIU, respectively. Due to the reverse movement, the total sensitivity of two dips can reach 141.6°/RIU. We compare the proposed device with previously reported devices in Table 2. The comparison result shows that our structure has a better performance.

Tab. 1　Sensitivities and FOMs with different refractive indices

n	1.33	1.38	1.43	1.48	1.53
S_A/(°)·RIU^{-1}	39.2	37.4	34.8	33.2	32.4
S_B/(°)·RIU^{-1}	102.4	95.4	83.4	74.2	70
S/(°)·RIU^{-1}	141.6	132.8	118.2	107.4	102.4
FOM$_A$/RIU^{-1}	115.2	104.0	91.8	85.6	82.9
FOM$_B$/RIU^{-1}	214.1	213.7	185.9	172.3	167.3

Tab. 2　Comparison of the proposed structure with previously reported devices

Structure	Sensitivity/(°)RIU^{-1}	Reference
Metallic nano-slit arrays	141.6	This work
Graphene-MoS_2-TiO_2-SiO_2	85.375	[39]
DBL-XMene-FG	64	[40]
ZnO and bi-metallic (Ag-Au) layers	116.67	[41]
Gate-controlled graphene sensor	108	[42]

Because of the narrow width and poor molecular mobility in the slit area, we consider two conditions in Fig. 6 (color online). In condition 1, the refractive index of the slit region is consistent with sensing medium. While in condition 2, the refractive index of the slit region is fixed at 1.33. The comparison result on the right of Fig. 6 shows that in these two cases, the positions of the four dips are nearly identical. Because the variation of the slit medium only affects the resonant wavelength of magnetic surface plasmon which is independent of incident angle. And the positions of four coherence dips mainly depend on the refractive index of the upper medium. Therefore, the inconsistency between the refractive index of slit region and upper medium has few influences on the sensing performance of this type of sensor.

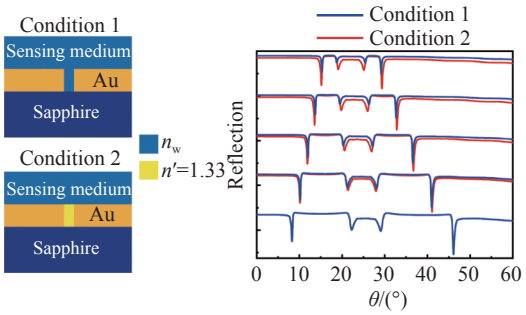

Fig. 6　Sensing performance comparison in two conditions. Condition 1: the refractive index of the medium in the slit is the same as that of the upper medium; condition 2: the refractive index of the medium in the slit is fixed at 1.33

Comparing coherence of surface plasmons in this structure (described by Eq. (1)) with lattice diffraction, such as X-ray diffraction (described by Bragg's theorem, $2d\sin\theta = m\lambda$), there are some differences between them. First, only relative phase difference is considered in lattice diffraction. Besides, the retardation effect related to the interaction of surface plasmon must be considered in the coherence of surface plasmons. As a result, the coherence dips manifest opposite movement in refractive index sensing.

4　Conclusion

In summary, we study the coherence of magnetic surface plasmon resonance in periodic metal nano-slit arrays and propose a convenient and high-accuracy sensing method. The coherence equations of surface plasmons in the structure are obtained by analyzing the correlated phase difference, and they are verified in 2D reflection spectrum. Due to the retardation effect, the two coherence dips in angle-resolved spectrum can move oppositely as the refractive index of the sensing medium changes. For sensing applications, compared with one dip used for sensing, two inversely moving dips can improve the sensitivity much more efficiently. In addition, the inconsistency between the refractive index of slit

medium and upper medium has few influences on the sensing performance, which can lead to wide practical applications.

References:

[1] KOYA A N, ZHU X CH, OHANNESIAN N, *et al*.. Nanoporous metals: from plasmonic properties to applications in enhanced spectroscopy and photocatalysis[J]. *ACS Nano*, 2021, 15(4): 6038-6060.

[2] HE ZH H, XUE W W, CUI W, *et al*.. Tunable fano resonance and enhanced sensing in a simple Au/TiO_2 hybrid metasurface[J]. *Nanomaterials*, 2020, 10(4): 687.

[3] PALERMO G, SREEKANTH K V, MACCAFERRI N, *et al*.. Hyperbolic dispersion metasurfaces for molecular biosensing[J]. *Nanophotonics*, 2021, 10(1): 295-314.

[4] AHMADIVAND A, GERISLIOGLU B, RAMEZANI Z, *et al*.. Functionalized terahertz plasmonic metasensors: femtomolar-level detection of SARS-CoV-2 spike proteins[J]. *Biosensors and Bioelectronics*, 2021, 177: 112971.

[5] SHEN B L, LIU L W, LI Y P, *et al*.. Nonlinear spectral-imaging study of second- and third-harmonic enhancements by surface-lattice resonances[J]. *Advanced Optical Materials*, 2020, 8(8): 1901981.

[6] GUAN J, SAGAR L K, LI R, *et al*.. Quantum dot-plasmon lasing with controlled polarization patterns[J]. *ACS Nano*, 2020, 14(3): 3426-3433.

[7] DORRAH A H, CAPASSO F. Tunable structured light with flat optics[J]. *Science*, 2022, 376(6591): eabi6860.

[8] PANDEY P S, RAGHUWANSHI S K, KUMAR S. Recent advances in two-dimensional materials-based kretschmann configuration for SPR sensors: a review[J]. *IEEE Sensors Journal*, 2022, 22(2): 1069-1080.

[9] XUE T Y, LIANG W Y, LI Y W, *et al*.. Ultrasensitive detection of miRNA with an antimonene-based surface plasmon resonance sensor[J]. *Nature Communications*, 2019, 10(1): 28.

[10] BAGHBADORANI H K, BARVESTANI J. Sensing improvement of 1D photonic crystal sensors by hybridization of defect and Bloch surface modes[J]. *Applied Surface Science*, 2021, 537: 147730.

[11] LIU F X, SONG B X, SU G X, *et al*.. Sculpting extreme electromagnetic field enhancement in free space for molecule sensing[J]. *Small*, 2018, 14(33): 1801146.

[12] CATTONI A, GHENUCHE P, HAGHIRI-GOSNET A M, *et al*.. λ^3/1000 plasmonic nanocavities for biosensing fabricated by soft UV nanoimprint lithography[J]. *Nano Letters*, 2011, 11(9): 3557-3563.

[13] MAYER K M, HAFNER J H. Localized surface plasmon resonance sensors[J]. *Chemical Reviews*, 2011, 111(6): 3828-3857.

[14] NUGROHO F A A, ALBINSSON D, ANTOSIEWICZ T J, *et al*.. Plasmonic metasurface for spatially resolved optical sensing in three dimensions[J]. *ACS Nano*, 2020, 14(2): 2345-2353.

[15] BUKASOV R, SHUMAKER-PARRY J S. Highly tunable infrared extinction properties of gold nanocrescents[J]. *Nano Letters*, 2007, 7(5): 1113-1118.

[16] HOU Y M. Coherence of magnetic resonators in a metamaterial[J]. *AIP Advances*, 2013, 3(12): 122119.

[17] HOU Y M. Interaction of magnetic resonators studied by the magnetic field enhancement[J]. *AIP Advances*, 2013, 3(12): 122118.

[18] KRAVETS V G, SCHEDIN F, GRIGORENKO A N. Extremely narrow plasmon resonances based on diffraction coupling of localized plasmons in arrays of metallic nanoparticles[J]. *Physical Review Letters*, 2008, 101(8): 087403.

[19] LIMONOV M F, RYBIN M V, PODDUBNY A N, *et al*.. Fano resonances in photonics[J]. *Nature Photonics*, 2017, 11(9): 543-554.

[20] LIMONOV M F. Fano resonance for applications[J]. *Advances in Optics and Photonics*, 2021, 13(3): 703-771.

[21] XIAO SH Y, WANG T, LIU T T, *et al*.. Active metamaterials and metadevices: a review[J]. *Journal of Physics D:Applied Physics*, 2020, 53(50): 503002.

[22] WANG B Q, YU P, WANG W H, *et al*.. High-Q plasmonic resonances: fundamentals and applications[J]. *Advanced Optical Materials*, 2021, 9(7): 2001520.

[23] UTYUSHEV A D, ZAKOMIRNYI V I, RASSKAZOV I L. Collective lattice resonances: plasmonics and beyond[J]. *Reviews in Physics*, 2021, 6: 100051.

[24] KRAVETS V G, KABASHIN A V, BARNES W L, *et al*.. Plasmonic surface lattice resonances: a review of properties

and applications[J]. *Chemical Reviews*, 2018, 118(12): 5912-5951.

[25] DONG J W, CHEN SH, HUANG G F, *et al*.. Low-index-contrast dielectric lattices on metal for refractometric sensing[J]. *Advanced Optical Materials*, 2020, 8(21): 2000877.

[26] CHEN J, ZHANG Q, PENG CH, *et al*.. Optical cavity-enhanced localized surface plasmon resonance for high-quality sensing[J]. *IEEE Photonics Technology Letters*, 2018, 30(8): 728-731.

[27] LIANG L, ZHENG Q L, WEN L, *et al*.. Miniaturized spectroscopy with tunable and sensitive plasmonic structures[J]. *Optics Letters*, 2021, 46(17): 4264-4267.

[28] WANG H, WANG X L, YAN CH, *et al*.. Full color generation using silver tandem nanodisks[J]. *ACS Nano*, 2017, 11(5): 4419-4427.

[29] DAQIQEH REZAEI S, DONG ZH G, YOU EN CHAN J, *et al*.. Nanophotonic structural colors[J]. *ACS Photonics*, 2021, 8(1): 18-33.

[30] SHI X ZH, CHEN CH SH, LIU S H, *et al*.. Nonvolatile, reconfigurable and narrowband mid-infrared filter based on surface lattice resonance in phase-change $Ge_2Sb_2Te_5$[J]. *Nanomaterials*, 2020, 10(12): 2530.

[31] MURAVITSKAYA A, GOKARNA A, MOVSESYAN A, *et al*.. Refractive index mediated plasmon hybridization in an array of aluminium nanoparticles[J]. *Nanoscale*, 2020, 12(11): 6394-6402.

[32] SHEN Y, ZHOU J H, LIU T R, *et al*.. Plasmonic gold mushroom arrays with refractive index sensing figures of merit approaching the theoretical limit[J]. *Nature Communications*, 2013, 4(1): 2381.

[33] LINDEN S, ENKRICH C, WEGENER M, *et al*.. Magnetic response of metamaterials at 100 terahertz[J]. *Science*, 2004, 306(5700): 1351-1353.

[34] ZHU Y H, ZHANG H, LI D M, *et al*.. Magnetic plasmons in a simple metallic nanogroove array for refractive index sensing[J]. *Optics Express*, 2018, 26(7): 9148-9154.

[35] CHEN J, FAN W F, ZHANG T, *et al*.. Engineering the magnetic plasmon resonances of metamaterials for high-quality sensing[J]. *Optics Express*, 2017, 25(4): 3675-3681.

[36] CHEN X SH, PARK H R, LINDQUIST N C, *et al*.. Squeezing millimeter waves through a single, nanometer-wide, centimeter-long slit[J]. *Scientific Reports*, 2014, 4(1): 6722.

[37] RHIE J, LEE D, BAHK Y M, *et al*.. Control of optical nanometer gap shapes made via standard lithography using atomic layer deposition[J]. *Journal of Micro/Nanolithography, MEMS, and MOEMS*, 2018, 17(2): 023504.

[38] JOHNSON P B, CHRISTY R W. Optical constants of the noble metals[J]. *Physical Review B*, 1972, 6(12): 4370-4379.

[39] HOSSAIN M B, RANA M M, ABDULRAZAK L F, *et al*.. Design and analysis of graphene–MoS_2 hybrid layer based SPR biosensor with TiO_2–SiO_2 nano film for formalin detection: numerical approach[J]. *Optical and Quantum Electronics*, 2019, 51(6): 195.

[40] PANDEY P S, SINGH Y, RAGHUWANSHI S K. Theoretical analysis of the LRSPR sensor with enhance FOM for low refractive index detection using MXene and fluorinated graphene[J]. *IEEE Sensors Journal*, 2021, 21(21): 23979-23986.

[41] MUDGAL N, SAHARIA A, AGARWAL A, *et al*.. ZnO and Bi-metallic (Ag–Au) layers based surface plasmon resonance (SPR) biosensor with $BaTiO_3$ and graphene for biosensing applications[J]. *IETE Journal of Research*, 2020: 1-8.

[42] HOSSAIN M M, TALUKDER M A. Gate-controlled graphene surface plasmon resonance glucose sensor[J]. *Optics Communications*, 2021, 493: 126994.

Author Biographics:

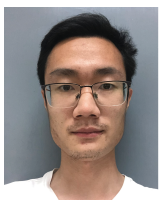

Yang Zong-meng (1996—), male, born in Daqing, Heilongjiang province, is now a master candidate in the School of physics, Beijing University, maily engaged in the research of coherence of surface plasmons. E-mail: zemelyang@pku.edu.cn

Hou Yu-min, female, born in Weifang, Shandong Province, Ph.D, now is a asoociate professor in the School of physics, Beijing University, mainly engaged in the research of surface plasmons recently. E-mail: ymhou@pku.edu.cn